ChemPhysChem

Research Article
doi.org/10.1002/cphc.202200621

Chemistry Europe
European Chemical Societies Publishing

www.chemphyschem.org

In Silico Partial N_2 to NH_3 Conversion with a Light Atom Molecule

Stefan Mebs*[a]

N_2 can be stepwise converted *in silico* into one molecule NH_3 and a secondary amide with a bond activator molecule consisting only of light main group elements. The proposed N_2-activating pincer-related compound carries a silyl ion ($Si^{(+)}$) center as well as three Lewis acidic (–BF_2) and three Lewis basic (–PMe_2) sites, providing an efficient binding pocket for gaseous N_2 within the framework of intramolecular frustrated Lewis pairs (FLP). In addition, it exhibits supportive secondary P–B and F···B contacts, which stabilize the structure. In the $PSi^{(+)}$–N–N–BP environment the N≡N triple bond is extended from 1.09 Å to remarkable 1.43 Å, resembling a N–N single bond. The strongly activated N–N-fragment is prone to subsequent hydride addition and protonation steps, resulting in the energy efficient transfer of two hydrogen equivalents. The next hydride added causes the release of one molecule NH_3, but leaves the ligand system as poisoned $R_3Si^{(+)}$–NH_2–PMe_2 or $R_3Si^{(+)}$–NH_3 dead-end states behind. The study indicates that approximately tetrahedral constrained $SiBP_2$-pockets are capable to activate N_2, whereas the acid-rich SiB_3- and SiB_2P-pocktes, as well as the base-rich SiP_3-pockets fail, hinting towards the high relevance of the acid-base proportion and relative orientation. The electronic structure of the N_2-activated state is compared to the corresponding state of a recently published *peri*-substituted bond activator molecule featuring a $PSi^{(+)}$–N–N–$Si^{(+)}$P site (S. Mebs, J. Beckmann, *Physical Chemistry Chemical Physics* **2022**, *24*, 20953–20967).

Introduction

Small molecule activation is a key aspect in all areas of (bio)chemical sciences as it plays an equally central role in biological evolution and industrial catalysis, particularly regarding the geopolitical and ecologic relevance of generation and storage of renewable energy by water oxidation and CO_2 reduction to produce "green hydrogen" and other valuable products.[1,2] Nitrogen fixation, activation, splitting, and ultimately conversion into two ammonia molecules is at the heart of this science as it delivers all bio-accessible nitrogen on the planet, on the one hand biosynthetically by nitrogenases and on the other technically by the Haber-Bosch process, the latter consuming 1–2% of the global industrial energy and causing 2–3% of the global industrial CO_2-production.[3–5] Heterogeneous N_2 to $2NH_3$ conversion was since decades studied experimentally and computationally for a plethora of cluster and network structures[6–18] and finally realized also in homogeneous catalysis, employing small transition-metal containing compounds, although in low efficiencies so far.[19–25] Attempts to replace the transition metals resulted in the first boron-based bimolecular catalysts within the framework of frustrated Lewis pairs (FLP) or by exploiting the ambiphilic nature of the boron atom having empty and filled orbitals under certain conditions (being in the $B^{(I)}$ instead of the common $B^{(III)}$ state, Scheme 1).[26–37] A recent computational study employed 2,3′-bipyridine to mediate intramolecular tetraboration of dinitrogen.[36] In a conceptual density functional theory (DFT) study on a *peri*-substituted bond activator molecule, we could recently show that N_2-splitting could potentially also be conducted intra-molecularly by tripodal light atom molecules containing only earth abundant C, H, P, and Si atoms.[38] Simpler molecular systems combining a silyl cation with a phosphine group are capable to activate the C–F bond.[27] Unfortunately, the previous tripod-systems are only capable to accomplish two of the four crucial steps on the way from gaseous N_2 to $2NH_3$: 1. Fixation and activation of N_2, 2. Splitting of the N≡N triple bond, 3. Release of one molecule NH_3, 4. Release of the second molecule NH_3.[38] Since these *peri*-substituted compounds contain two silyl cations in which N_2 is stiffly bound within a $PSi^{(+)}$–N–N–$Si^{(+)}$P pocket, the pre-final R_3Si–NH_3 states, in which both NH_3 are bound to $Si^{(+)}$, have to be considered as poisoned dead-end states. Attempts to replace the strongly electrophilic silyl cations by less strong boron atoms (e.g. as –BF_2 groups) failed for this compound class. In addition, the structure contains bulky acenaphthyl backbone fragments, as well as bulky –$SiPh_2$ and –PPh_2 side groups, potentially hampering gaseous N_2 to access the binding pocket ("active site"). Two modifications are thus implemented in our new molecular design to address these issues, which, however, still should follow the basic approach to be principally accessible by means of synthetic chemistry. Instead of the bulky backbones and side groups, we use here a smaller pincer-related ligand system (Scheme 1) and the –$Si^{(+)}Ph_2$ group is replaced by –BF_2 groups. Replacing –PPh_2 by –PMe_2 is not realistic in the laboratory, since organic dimethyl-phosphines

[a] S. Mebs
Institut für Experimentalphysik
Freie Universität Berlin
Arnimallee 14, 14195 Berlin, Germany
E-mail: stefan.mebs@fu-berlin.de

Supporting information for this article is available on the WWW under https://doi.org/10.1002/cphc.202200621

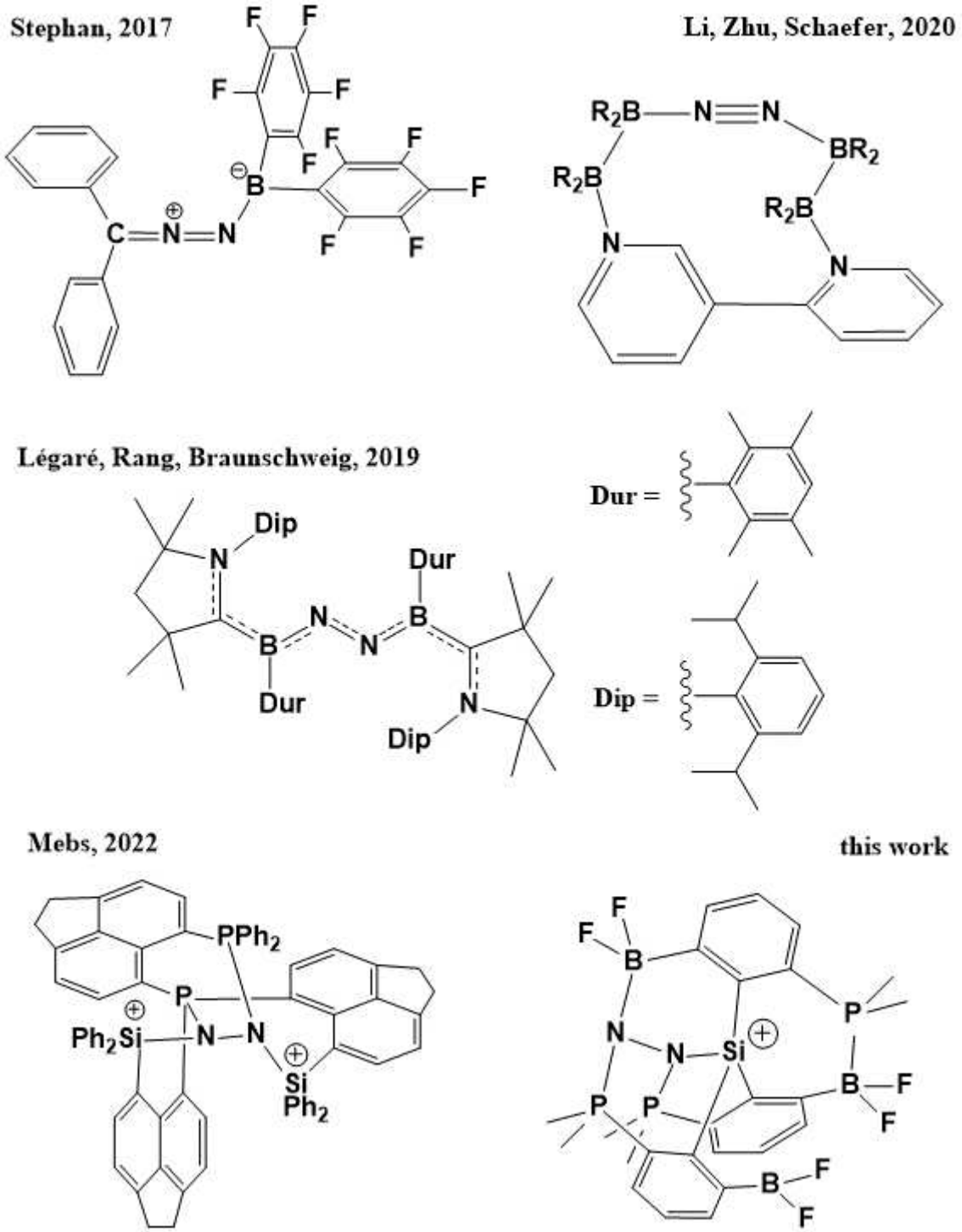

Scheme 1. Activation of N_2 by intermolecular frustrated Lewis pairs, hypovalent borylene compounds, diboranes, and intramolecular frustrated Lewis pairs using *peri*-substituted or pincer-related bond activator systems.

are often pyrophoric and toxic gases, but was done here *in-silico* to significantly reduce computational efforts. For the same reason, the study was conducted using a smaller basis-set size than previously,[38] *vide infra*. Since the energetic trends were identical for both levels of theory in our first study and the methyl groups are located at the outer areas of the pincer-related molecules, likely neither affecting N_2 uptake nor subsequent chemical transformations, both simplifications seem justified. Another simplification relates to the reaction scheme. It is not feasible in a hand-designed computational study to consider all potential attack sites for protons (including N or P atoms) and hydride ions (including N or B atoms) in each

reaction step in such complex ligand systems, but we nevertheless attempted to thoroughly trace back all likely candidates and routes in our study. In the course of finding the most probable route, we focused on two aspects: 1. Although adding multiple $H^{(+)}$ or $H^{(-)}$ ions successively or simultaneously is not fully excluded, we expected (and found) an iterative $H^{(-)}$–$H^{(+)}$–$H^{(-)}$–$H^{(+)}$... route to be the most promising reaction scheme, being somewhat reminiscent to transfer of hydrogen equivalents *via* proton-coupled electron transfers (PCETs) in nature, starting with adding hydride as initial reduction step; 2. Once a clearly preferred binding site for $H^{(+)}$ or $H^{(-)}$ ions was observed, e.g. at N(2), we focused on the further stepwise reduction/protonation of that site and excluded other potential side-path. It can thus not be fully excluded that a potentially relevant side-branch of the reaction scheme was missed. All-in-all, 44 structures have been optimized for that scheme, supplemented by calculations of structural variants and a potential energy scan of the N_2-adduct. In our first N_2-related DFT study we focused on N_2 uptake and activation with the goal to finally break the N≡N triple bond and on describing in detail the different structural motifs / electronic states using a variety of qualitative and quantitative real-space bonding indicators (RSBIs), including Atoms-In-Molecules (AIM[39–41]) bond topology, non-covalent interactions index (NCI[42]) contact-patterns, and electron localizability indicator (ELI-D[43]) representations.[38] In the current study we use the RSBIs to compare the N_2-activated state of the *peri*-substituted and pincer-related bond activator molecules.

Methods Section

Structural optimizations were conducted at the curta supercomputer system of the Freie Universität Berlin for 49 models applying density functional theory (DFT) at the b3pw91-D3/6-31+G*[44,45] level of theory using Gaussian16, [46] two of which failed to converge, see below and in the Supporting Information. London dispersion was modelled using Grimme's GD3BJ parameters (b3pw91-D3)[47] and the dichloromethane environment was mimicked by the COSMO solvation model.[48] Subsequent normal mode (or frequency) analysis proved all but two of the optimized structures to be local minima; models **1b** or **6g** have negative frequencies at −26 or −34 cm^{-1}, which represent negligible phononic bands. Attempts to re-optimize those two structures in order to find lower energy states failed. ΔG values were extracted and used to set up a potential reaction scheme for partial N_2-to-NH_3-conversion. The ΔG value of the crucial N_2-adduct formation step was corrected twofold: First, the conversion from 1 atm standard state (ΔG°_{atm}) to the 1 M standard state (ΔG°_{M}) was done using $\Delta G^{\circ}_{M} = \Delta G^{\circ}_{atm} + R_1 T \ln(R_2 T^{\Delta n})$ with $R_1 = 8.31447\ J\,K^{-1}\,mol^{-1}$, $R_2 = 0.08206\ L\,atm\,K^{-1}\,mol^{-1}$, T = temperature in K, and n = change in number of moles,[49] causing a free enthalpy expense of 7.9 $kJ\,mol^{-1}$. Second, the basis-set superposition error (BSSE) was estimated by counterpoise correction for the most relevant states. A potential energy scan (PES) was conducted for the N_2-adduct for a series of fixed N–N distances between 1.10 and 1.55 Å in 0.05 Å steps in order to disclose a potential transition state geometry. Moreover, the electronic structure of the lowest-energy N_2-adduct was analyzed. The wavefunction (wfn) file was used for a topological analysis of the electron density according to the Atoms-In-Molecules (AIM[39–41]) space-partitioning scheme using AIM2000; [50] DGRID-5-1[51] was used to generate and analyze the Electron-Localizability-Indicator (ELI-D[43]) related real-space bonding descriptors applying a grid step size of 0.05 a.u. using the formatted checkpoint file (fchk). For ELI–D figures, additional grids of 0.12 a.u. step size were computed. NCI[42] grids were generated with NCIplot[52] for a grid step-size of 0.12 a.u. Structures are displayed with ChemCraft,[53] bond paths are displayed with AIM2000, NCI figures are displayed with VMD, [54] and ELI–D figures are displayed with MolIso.[55] AIM topology transcends the Lewis picture of chemical bonding as it also includes secondary intramolecular interactions. In addition, it provides atomic and fragmental charges and volumes. NCI discloses (extended) contact patches of non-covalent interactions. ELI–D, nicely complementing NCI,[56] discloses shapes and sizes of localized electron pair basins, e.g. core, bonding, or lone-pair, and the electron populations of those basins.

Results and Discussion

Due to the complexity of the investigated structures, we use a specific nomenclature which should ease reading. According to this labeling scheme, the neutral starting state (or the R_3SiH ligand system, R = 2-dimethylphosphino-6-difluoroborano-phenyl) is given the number **0**, the single positive charged silyl ion "active state" after hydride abstraction is denoted as **1**, all following states directly refer to the number of atoms added to the compound, e.g. **2** refers to the N_2-adduct (two extra atoms), **3** to the $N_2 + H^{(-)}$-state (three extra atoms), and so on. Accordingly, the last state, **8**, refers to the addition of eight extra atoms, formally $N_2 + 3H_2$. Structural isomers of the same electronic state are highly relevant in this study; particularly regarding unwanted formation of dead-end states; they are denoted by small letters behind the number, e.g. **0a–d**. The lowest energy or most reasonable isomer of each electronic state is displayed in the proposed reaction scheme for the "main route" towards NH_3 (see Figure 1 for structures and Figure 2 for free enthalpies), for simplicity only by their numbers, e.g. **0** instead of **0b**, etc. In the main text, the isomers which are part of the proposed main route are accordingly labeled in a **0b(0)** like fashion. In figures and tables, reduction steps *via* adding hydride are colored blue, whereas protonation steps are colored red.

Synthesis of **0** (the ligand system) can result in four different structural isomers depending on the relative location of the three Lewis acid (LA, 'A', $-BF_2$) and base (LB, 'B', $-PMe_2$) sites as well as the relative orientation of the Si–H part, see Scheme 2, Figure 1 and Figure S1 in the Supporting Information. Defining a virtual plane through the three C atoms forming the Si–C bonds, the following conformations are possible: BBA–SiH–AAB (**0a**), BBA–HSi–AAB (**0b(0)**), BBB–SiH–AAA (**0c**), and

Research Article
doi.org/10.1002/cphc.202200621

Chemistry Europe
European Chemical Societies Publishing

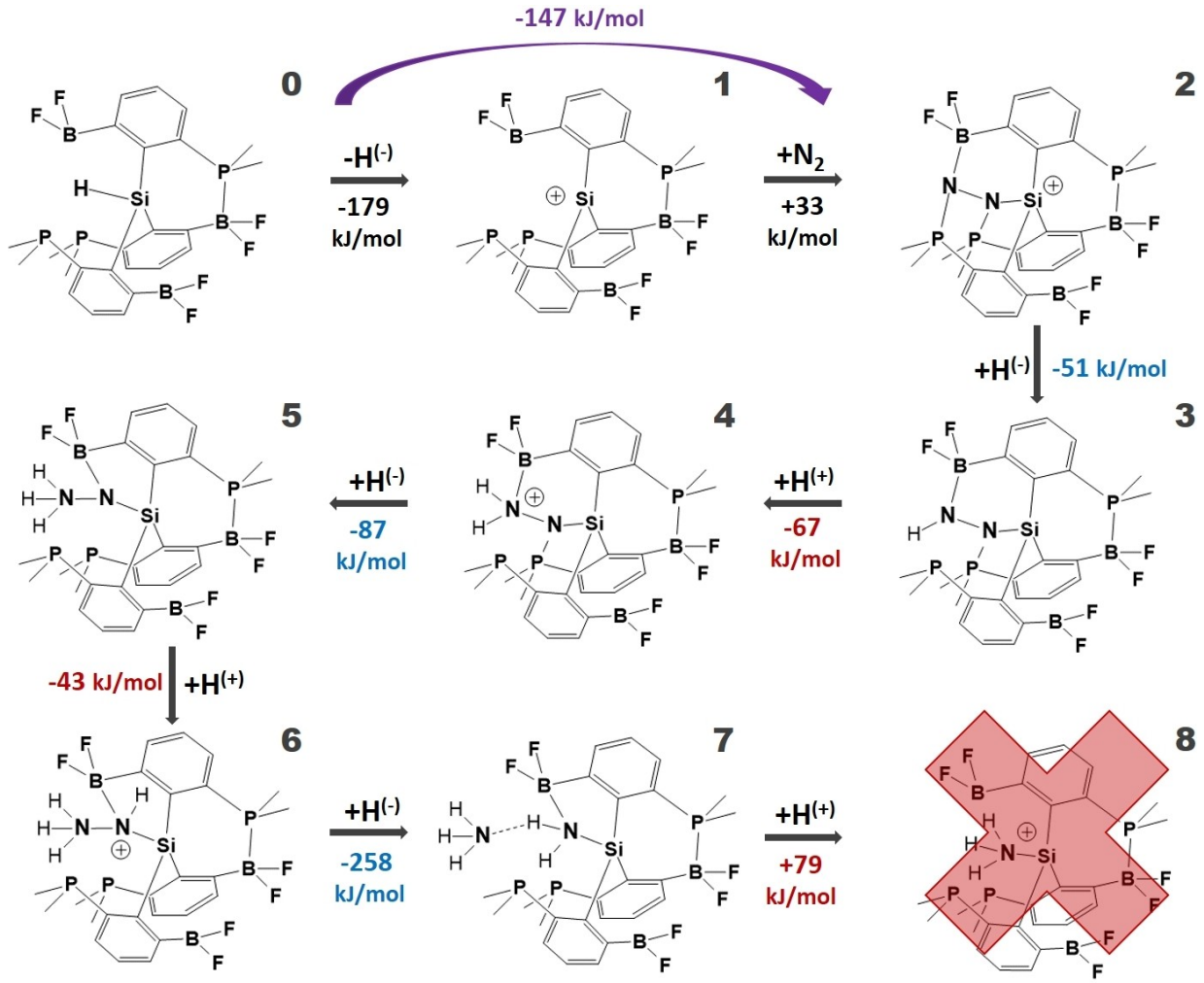

Figure 1. Proposed main route for possible N_2-uptake, subsequent proton-balanced reduction (transfer of hydrogen equivalents), and partial release of ammonia (one molecule). **0**: lowest energy neutral starting state. **1**: Quenched "Active state" after hydride abstraction. **2**: N_2-activated state. **3**: Adding hydride at N(2). **4**: Adding proton at N(2). **5**: Adding hydride at N(2). **6**: Adding proton at N(1). **7**: Adding hydride at N(1). **8**: Adding proton at N(1). The ΔG value for N_2-adduct formation (+33 kJ mol^{-1}, step **1**→**2**) is corrected for 1 atm→1 M standard state (+7.9 kJ mol^{-1}) and basis-set superposition error (BSSE, +22.5 kJ mol^{-1}), see Figure 2 for the corresponding enthalpy diagram. The ΔG value of −258 kJ mol^{-1} (step **6**→**7**) is corrected for attractive $H_3N^{\cdot\cdot}H_2N$ interaction (−40.5 kJ mol^{-1}) in **7**. Color code enthalpies: hydride abstraction and subsequently adding N_2 – black, hydride abstraction *via* purging with N_2 – purple, adding hydride – blue, adding proton – red.

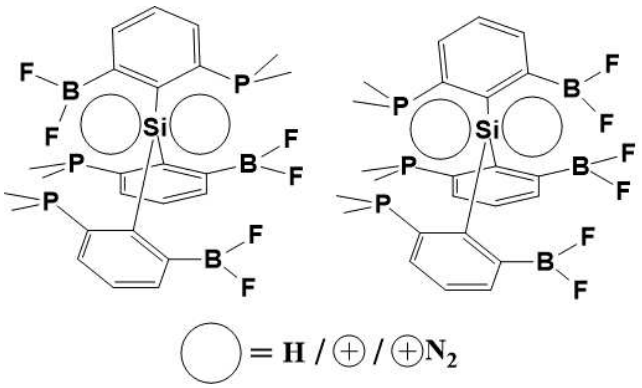

Scheme 2. Schematic representation of possible structural variants of BBA–Si$^{(+)}$–AAB (**1 a(1)**) or BBB–Si$^{(+)}$–AAA (**1 b**). The four potential binding pockets for N_2 ("active sites") are highlighted by circles.

BBB–HSi–AAA (**0 d**). The less symmetric **0 a** and **0 b(0)** are favored by ΔG = 20–30 kJ mol^{-1} over the more symmetric **0 c** and **0 d**, because both form one short Lewis pair -Me_2P–BF_2- contact ($d_{(P,B)}$ = 2.092 Å in **0 a** and 2.070 Å in **0 b(0)**) (Table S2). For all four isomers of state **0**, hydride abstraction using $Ph_3C^{(+)}$ to form BBA–Si$^{(+)}$–AAB (**1 a(1)**) or BBB–Si$^{(+)}$–AAA (**1 b**) and Ph_3CH is strongly exergonic (ΔG = −150 to −190 kJ mol^{-1}, Table S6) as both cationic ligand systems exhibit three strong intra-molecular secondary interactions (Figure S1). **1 a(1)** forms a P–Si bond ($d_{(P,Si)}$ = 2.280 Å) and two P–B bonds ($d_{(P,B)}$ = 2.063 and 2.066 Å), whereas **1 b** forms three P–Si bonds ($d_{(P,Si)}$ = 2.533, 2.535, 2.535 Å). These short contacts make the structural isomers of **1** rather quenched dead-end states than "active" states, which is a setback as hydride abstraction is a prerequisite for activating the ligand system in order to fix gaseous N_2. Additionally, potential intra-molecular fluoride abstraction from a –BF_2 side

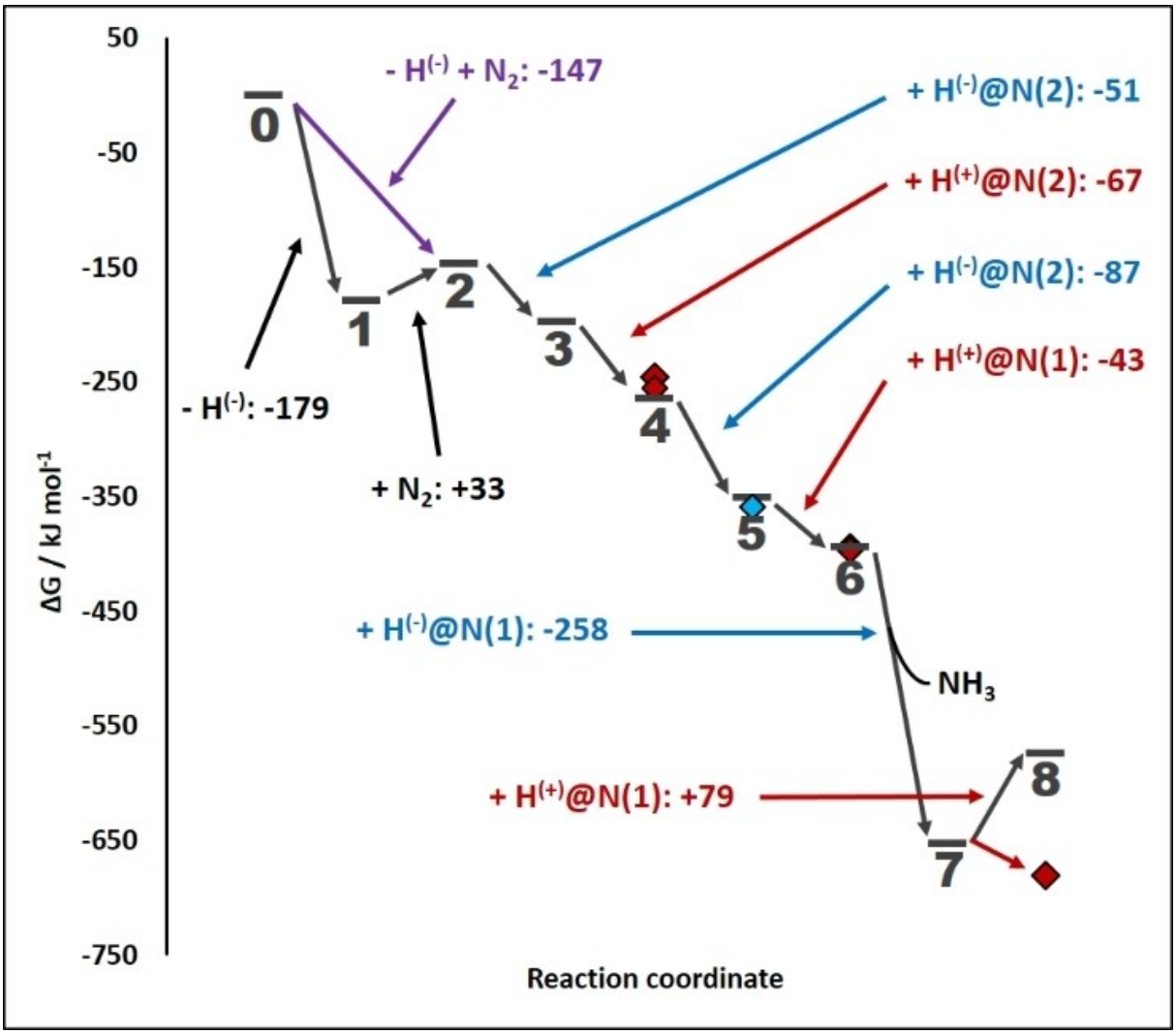

Figure 2. Enthalpy diagram of proposed main route for possible N_2-uptake, subsequent proton-balanced reduction (transfer of hydrogen equivalents), and partial release of ammonia (one molecule). State **2** is corrected for 1 atm→1 M, as well as for BSSE (see Figure S9 for further details). State **7** is corrected for attractive $H_3N\cdots H_2N$ interaction. Color code enthalpies: hydride abstraction and subsequently adding N_2 – black, hydride abstraction *via* purging with N_2 – purple, adding hydride – blue, adding proton – red. Higher energy quenching states after initial hydride abstraction (e.g. by partial fluoride abstraction) are represented as green rhombi. Undesired protonation of $-PMe_2$ groups is represented as red rhombi. The blue rhombus represents adding hydride at N(1) instead of N(2).

group by the silyl cation to form Si–F and $-{}^{(+)}BF$ groups was addressed for different variants of **1 a(1)** and **1 b**, which resulted in higher energy structures for **1 a(1)** (→**1 c**, **1 d**; Figure S2), or the starting Si–F dead-end structures returned to **1 b** *via* structural relaxation, excluding these detrimental side-paths. Notably, **1 a(1)** and **1 b** together provide four different types of binding pockets for N_2 (Scheme 2): Counting the central Si cation as Lewis acid (A), **1 a(1)** has an A_2B_2- and an A_3B-pocket, whereas **1 b** has an AB_3- and an A_4-pocket. Adding N_2 to the two isomers of state **1** thus answers two questions: a) are the "active" states still capable to fix N_2? b) if yes, which is the most efficient A : B-ratio for N_2-fixation? For **1 b**, both N_2-adduct optimizations failed as N_2 disappears from the binding pockets (not shown), excluding the Lewis acid rich A_4-site and the Lewis base rich AB_3-site from N_2-activation. For **1 a(1)**, both optimizations succeeded (Figure S3), resulting in a strongly endergonic N_2-adduct formation process for the Lewis acid rich A_3B-site ($\Delta G = +239\ kJ\,mol^{-1}$, **2 b**), but only a slightly endergonic reaction for the A_2B_2-site ($\Delta G = +33\ kJ\,mol^{-1}$, **2 a(2)**). Consequently, a solution of the starting compound **0** has to be purged with N_2-gas *via* the hydride abstraction step in order to circumvent formation of state **1** and go directly from state **0** to state **2**, and in addition, N_2-fixation will only occur in the binding pocket containing two Lewis acids ($Si^{(+)}$ and B) and two Lewis bases (both P). Notably, the free enthalpy of this reaction **0 b(0)**→**2 a(2)** is strongly exergonic ($\Delta G = -147\ kJ\,mol^{-1}$, purple arrow in Figure 1).

Adding the first hydride to the N_2-activated state **2 a(2)** either at N(1) (**3 a**) or N(2) (**3 b(3)**) immediately results in the release of one PMe_2 group, i.e. one of the two P–N bonds is

broken (Figures 1 and S3), which wasn't observed in the recently published $Si_2^{(2+)}P_2$-variants.[38] We suspect that this circumstance likely makes later NH_3-release also easier in the here presented $Si^{(+)}BP_2$-variants. Accordingly, adding the second hydride in a later step breaks the second P–N bond, *vide infra*. However, it also opens the $-PMe_2$ groups for later attack by protons, which causes the formation of unwanted side-products, potentially hampering further N_2-reduction. Generally, the formation of detrimental B–H side products *via* adding hydride is much less likely than the formation of P–H side products *via* protonation due to the energetic cost of rehybridization transforming a planar $C_{ring}BF_2$- into a tetrahedral $C_{ring}BF_2H$-group. Formation of **3b(3)** ($\Delta G = -50.6$ kJ mol^{-1}) is strongly favored over **3a** ($\Delta G = -4.3$ kJ mol^{-1}) or **3c** ($\Delta G = +1.9$ kJ mol^{-1}, unwanted B–H side product), thus **2a(2)**→**3b(3)** is considered as main route. We nevertheless calculated the subsequent protonation at N(1), N(2), and at a neighboring P atom starting from the optimized structures of **3a** and **3b(3)**, resulting in six isomers of the electronic state **4**, now formally comprising one molecule N_2 and one molecule H_2 (Figures 1 and S4). The largest free enthalpy gain was obtained in the reaction **3b(3)**→**4d(4)** ($\Delta G = -67.2$ kJ mol^{-1}, $H^{(-)}$ and $H^{(+)}$ at N(2)), closely followed by unwanted protonation at the P atoms ($\Delta G = -59.0$ kJ mol^{-1} (**4f**) and -49.5 kJ mol^{-1} (**4e**)). With $\Delta G = -8$ to -23 kJ mol^{-1}, states **4a–c** are much less likely and thus not considered further.

Starting from **4d(4)**, the second hydride was added to N(1) (**5a**), N(2) (**5b(5)**), and a BF_2-group (**5c**), the first two being strongly favored ($\Delta G = -94.6$ and -86.6 kJ mol^{-1}) over the last one ($\Delta G = -17.4$ kJ mol^{-1}). As mentioned above, this causes release of the second $-PMe_2$-group (Figures 1 and S5). In addition, it causes a change in the bond topology for **5b(5)** as the N(2)–BF_2-bond is broken while a N(1)–BF_2 bond is formed. Although the N(1)-site is slightly preferred for second hydride addition over the N(2)-site by means of ΔG, we focus on the path **4d(4)**→**5b(5)** because the following step (second protonation) strongly prefers the route **5b(5)**→**6c(6)** ($\Delta G = -43.3$ kJ mol^{-1}), i.e. adding the second hydride at N(2) and then the second proton at N(1), over routes starting from **5a** ($\Delta G = -7.9$ (**6a**) and -6.5 (**6b**) kJ mol^{-1}, Figures 1 and S6). However, it has to be noted, that again proton attack of free $-PMe_2$ groups is also favored by $\Delta G = -44.3$ (**6d**) and -45.5 (**6e**) kJ mol^{-1}, so even if they won't fully hamper further N_2-reduction, they likely will reduce the yields. Electronic state **6** formally comprises one molecule N_2 and two molecules H_2.

Starting from **6c(6)**, carrying one H-atom at N(1) and three H-atoms at N(2), the third hydride was added to N(1) (**7a(7)**) or a free BF_2-group (**7b**), the latter again being energetically irrelevant ($\Delta G = -13.8$ kJ mol^{-1}). To our own surprise, adding the third hydride to N(1) caused the release of one NH_3-molecule in the optimization process and is strongly favored ($\Delta G = -258.3$ kJ mol^{-1}). **7c** represents the corresponding structurally optimized model lacking the released NH_3-molecule (Figure S7). At this point, the reaction scheme couldn't be extended to the release of the second NH_3-molecule, finally closing the cycle, because the NH_2-fragment is strongly bound as bridging secondary amine in a $Si^{(+)}$–NH_2–B-fashion. Formation of hypothetical structure **8a(8)** carrying a Si–NH_3 group is already strongly endergonic ($\Delta G = +78.7$ kJ mol^{-1}), so **7c** might be considered as poisoned dead-end state. The same is potentially true for **8a(8)**, even if it could be accessed, since it exhibits a strong Si–NH_3 bond. It should be noted, however, that the reaction **8a(8)** + N_2→**2a(2)** + NH_3 is formally exergonic ($\Delta G = -53.4$ kJ mol^{-1}).

Figures 1 and 2 display the structures and enthalpies of the reaction scheme, which we propose to be the most likely path from gaseous N_2 to one molecule NH_3 and the poisoned end-state ("main route"). Purging the lowest energy isomer of the neutral starting state **0b(0)** with N_2 *via* hydride abstraction ideally results in formation of **2a(2)**, releasing thereby 147 kJ mol^{-1}, and preventing formation of the quenched state **1a(1)**. Transfer of two hydrogen equivalents by stepwise adding hydride and subsequent protonation results in formation of **6c(6)**, exhibiting a R3$Si^{(+)}$–NH(NH_3) –BF_2R bonding environment, in which both $-PMe_2$ groups are already detached from the N_2-fragment. The yield of **6c(6)** depends on the relative amounts of unwanted protonation the released $-PMe_2$ groups (red rhombi in Figure 2), whereas unwanted H–BF_2 formation in the steps of adding hydride can probably be neglected. Adding the third hydride finally leads to the release of one molecule NH_3 and the remaining N atom within a R3$Si^{(+)}$–NH_2–BF_2R bonding environment, which most likely is a dead-end state. Figure S8 shows the reaction scheme using the optimized structural geometries instead of line-drawings as shown in Figure 1.

Formation of transferable "$H^{(-)}$" and "$H^{(+)}$" by heterolytic cleavage of H_2 according to the reaction scheme: $^1/_2B_2H_6 + Tf^{(-)} + H_2 \rightarrow BH_4^{(-)} + TfH$ requires: $\Delta G = 151.8$ kJ mol^{-1}, summing up to 455 kJ mol^{-1} for three hydrogen equivalents. Notably, the three pairs of reduction/protonation (transfer of one hydrogen equivalent) are considerably exergonic (-118, -130, -179 kJ mol^{-1}), resulting in an overall energy gain form state **2a(2)** to **8a(8)** of -427 kJ mol^{-1}, almost fully compensating the initial energy requirements of splitting H_2.

In order to understand, to what extend the dative Me_2P–BF_2 and rather ionic BF_2···BF_2 contacts at the opposite site of the molecule (orange arrows in Figures S1-7) are of relevance for N_2-activation, the electronic states **0**, **1**, and **2** were calculated for a smaller model compound containing only two $-PMe_2$ groups and one $-BF_2$ group (Figure S10), also building an A_2B_2-pocket. The critical step (**0**→**2**) is still exergonic ($\Delta G = -85$ kJ mol^{-1}; including an approximative ΔG expense of $+30$ kJ mol^{-1} for the 1 atm→1 M and BSSE corrections, the latter being calculated for the larger parent $SiBP_2$-system) but considerably less pronounced than for the parent system with three LA and LB sites ($\Delta G = -147$ kJ mol^{-1}). Moreover, the smaller model compound offers the possibility of rotational isomerism, including potential structures which do not form a proper binding pocket for N_2 anymore, highlighting the relevance of intra-molecular interactions *outside* the binding pocket for structural stability and N_2-adduct formation support. In order to understand, if the central $Si^{(+)}$ group could be replaced with a B atom, corresponding calculations were performed for the neutral B-centered ligand system, which of course lacks the initial "activation step" by hydride abstraction,

and the N_2-adduct (Figure S11). The neutral ligand system exhibits three short P–B bonds (2.015, 2.032, 2.063 Å), also involving the central B atom, blocking the binding pocket and making N_2-adduct formation considerably endergonic ($\Delta G = 65\ kJ\,mol^{-1}$; again including $+30\ kJ\,mol^{-1}$ as 1 atm→1 M and BSSE correction estimate), excluding the use of boron at the central position in this molecular system.

As in the recently published study on the related *peri*-substituted bond activator molecule[38] the potential energy scan (PES) on the N_2-adduct (**2a**), applying restrained optimizations for a series of structures with fixed N–N distances, shows a smooth decrease of the molecular energy from $d_{(N,N)} = 1.10$ Å to the minimum geometry at about 1.43 Å, and thus no indication for a transition state, suggesting that, once N_2 has entered the binding pocket/active site no further activation is needed (Figure S12).

Geometric and Electronic Structure of the N_2-Adduct

The studied pincer-related compound exhibits a $PSi^{(+)}$–N–N–BP configuration in the N_2-adduct (**2a(2)**), which stretches the N≡N triple bond energy efficiently from 1.09 to 1.43 Å, surprisingly being even 0.01 Å longer than in the corresponding state of the recently published *peri*-substituted bond activator complex which exhibits a highly charged $PSi^{(+)}$–N–N–$Si^{(+)}$P environment and serves as reference here.[38] The *peri*-substituted bond activator complex was optimized at two different levels of theory in the previous study, employing the larger 6–311+G(2df,p) and the smaller 6–31+G* basis-set, the latter one being also used here. Table 1 collects relevant bond distances and angles, as well as torsion angles of the N_2-containing binding pocket for all three models. It confirms that the difference in the N–N stretching between *peri*-substituted and pincer-related bond activator molecule is not due to the applied basis-set. Notably, the Si–N and one P–N bond in **2a(2)** are 0.05 and 0.02 Å shorter compared to the corresponding bonds in the reference (one P–N bond is similar), and of course is the B–N bond in **2a(2)** considerably shorter than a Si–N bond in the *peri*-substituted complex, suggesting overall slightly stronger bonding of the N atoms in **2a(2)** than in the reference, despite being located in a less high charged environment. Both compound types, *peri*-substituted and pincer-related bond activator complex, show similar deviations from the ideal tetrahedral Si–N–N or P–N–N angles (dev(109.5°)) and from the ideal tetrahedral Si/P–N–N–Si/P torsion angles (dev(90°)), so the surprisingly large N–N bond activation in **2a(2)** could rather be explained by the presumably smaller size of the binding pocket in the pincer-related compound, facilitating more efficient orbital overlap between the ligand system and N_2, than by the superior kind or better relative positions of LA and LB atoms, but this remains speculative at this point.

Table 1 also comprises a set of topological and integrated RSBIs for the N–N, P–N, Si–N, and B–N bonds of the N_2-activated states in the *peri*-substituted and pincer-related bond activator complexes, derived from the electron and electron-pair densities. The electron density (ED, $\varrho(\mathbf{r})_{bcp}$) at the bond critical point (bcp) as well as the respective curvature (Laplacian, $\nabla^2\varrho(\mathbf{r})_{bcp}$) and kinetic or total energy density over ED ratios ($G/\varrho(\mathbf{r})_{bcp}$, $H/\varrho(\mathbf{r})_{bcp}$) characterize the bonds to be weak or strong and covalent, polarized, or ionic. On a first glance, the bonding situation is quite similar for both N_2-adducts. The homo-polar N–N bonds exhibit high $\varrho(\mathbf{r})_{bcp}$ values (above 2 eÅ^{-3}), negative $\nabla^2\varrho(\mathbf{r})_{bcp}$ values (below −8 eÅ^{-5}), and $|H/\varrho(\mathbf{r})_{bcp}| > |G/\varrho(\mathbf{r})_{bcp}|$, qualifying them as strong and covalent. Bond ellipticities (ε) close to zero suggest a cylindrical shape of the ED distribution along the N–N axis, thus no bending. The relative position of the bcp along the N–N axis (d_1/d) close to 0.5 and the Raub-Jansen-Index (RJI)[57] of 50–55% confirms that the bond is still homo-polar within the adducts. The RJI quantifies the relative electron populations of one ELI–D basin (e.g. N–N bonding basin) within the two (or more) AIM-atoms it is overlapping with, thereby indicating bond polarization. Notably, the N atoms accumulate tremendous amounts of charge ($Q_{AIM}(E) = -1.3$ to -1.5 e) in the process of adduct formation. The considerably stretched N–N bond, however, causes the corresponding ELI–D basin to be very small ($V_{ELI} = 0.8$ Å^{-3}) and to contain only low electron populations of about 1.1 e (N_{ELI}). The high AIM atomic charge of the N atoms thus stems from the ELI–D basins of the P–N and Si/B–N basins, as well as from newly formed lone-pair-basins, see Figure S13 for details. The longer P–N, B–N, and Si–N bonds are characterized by lower $\varrho(\mathbf{r})_{bcp}$ values (below 1.3 eÅ^{-3}), positive $\nabla^2\varrho(\mathbf{r})_{bcp}$ values (3–14 eÅ^{-5}), and $|G/\varrho(\mathbf{r})_{bcp}| > |H/\varrho(\mathbf{r})_{bcp}|$, qualifying them as weaker and strongly polarized with increasingly dominant ionic bond contributions. Bond ellipticities of 0.1–0.2 suggest electron "smearing", thus slight bending. The bcp is closer to the less electronegative P, B, and Si atoms ($d_1/d = 0.3$–0.4), and the RJI determine those bonds to be polarized-covalent (P–N; RJI = 82-83%) or dative (B/Si–N; RJI = 93–95%). Notably, the ELI–D basins of the P–N bonds, which stem from the formerly lone-pair basins of the P atoms, are smaller (V_{ELI}), contain less electron populations (N_{ELI}), and have a lower localizability at the attractor position of the basin (γ_{ELI}) than the corresponding basins of the B/Si–N bonds, which stem from the formerly lone-pair basins of the N atoms in gaseous N_2. This indicates that, despite the tremendous changes in the electronic structure of the N–N bond *via* adduct formation, the initial character of P/N lone-pair basins is much less affected.

The topological bond paths motif of **2a** is displayed in Figure 3a. It indicates that weak intra-molecular secondary interactions, such as H·—·H contacts, play a minor role in stabilizing the binding pocket, whereas much stronger P–B and F·—·B interactions are visible at the other side of the molecule. This is supported by the NCI, which shows extended areas of non-covalent contact patches (Figure 3b). AIM topology and NCI patches will of course be altered by replacing the $-PMe_2$ groups, which are not accessible synthetically, by the larger $-PPh_2$ groups. At an ELI–D value of 1.3 (Figure 3c) the small and weak N–N bonding basin is topologically almost separated from the adjacent P/B/Si–N bonding and N lone-pair basins, whereas the latter types are still fused, suggesting that

Table 1. Geometric and electronic bond descriptors for two N_2-adducts.[a]

model	basis-set	N(1)–N(2)	Si(1)–N(1)	Si(2)/B(2)–N(2)	P(1)–N(1)	P(2)–N(2)
Si_2P_2	high	1.418	1.821	1.790	1.686	1.662
Si_2P_2	low	1.416	1.832	1.799	1.701	1.674
2 a(2)	low	1.428	1.773	1.587	1.664	1.667
model	basis-set	dev(109.5°) (angles)	Si(1)–N(1)–N(2)	Si(2)–N(2)–N(1)	P(1)–N(1)–N(2)	P(2)–N(2)–N(1)
Si_2P_2	high	−5.6	106.68	124.27	113.36	115.96
Si_2P_2	low	−5.6	106.77	124.20	113.11	116.26
2 a(2)	low	−4.4	113.54	116.00	122.96	102.99
model	basis-set	dev(90°) (torsion)	Si(1)–N(1)–N(2)–P(2)	Si(1)–N(1)–N(2)–Si(2)	P(1)–N(1)–N(2)–P(2)	P(1)–N(1)–N(2)–Si(2)
Si_2P_2	high	13.4	−100.61	106.22	71.32	−81.84
Si_2P_2	low	14.0	−101.24	106.68	70.95	−81.13
2 a(2)	low	18.8	−84.58	57.77	125.93	−91.71
Si_2P_2	d [Å]	$\varrho(\mathbf{r})_{bcp}$ [eÅ^{-3}]	$\nabla^2\varrho(\mathbf{r})_{bcp}$ [eÅ^{-5}]	ε	d_1/d	$Q_{AIM}(E)$
N(1)–N(2)	1.418	2.04	−8.7	0.01	0.50	−1.49/−1.43
P(1)–N(1)	1.686	1.24	3.9	0.19	0.39	2.70
P(2)–N(2)	1.662	1.29	5.8	0.19	0.39	2.77
Si(1)–N(1)	1.821	0.74	8.5	0.12	0.39	2.90
Si(2)–N(2)	1.790	0.78	9.6	0.13	0.40	2.89
2 a(2)	d [Å]	$\varrho(\mathbf{r})_{bcp}$ [eÅ^{-3}]	$\nabla^2\varrho(\mathbf{r})_{bcp}$ [eÅ^{-5}]	ε	d_1/d	$Q_{AIM}(E)$
N(1)–N(2)	1.428	2.02	−10.9	0.03	0.51	−1.50/−1.36
P(1)–N(1)	1.664	1.20	12.9	0.14	0.38	3.29
P(2)–N(2)	1.667	1.23	12.3	0.19	0.38	3.06
Si(1)–N(1)	1.773	0.77	14.1	0.10	0.39	2.93
B(2)–N(2)	1.587	0.93	6.9	0.10	0.32	2.31
Si_2P_2	$G/\varrho(\mathbf{r})_{bcp}$ [a.u.]	$H/\varrho(\mathbf{r})_{bcp}$ [a.u.]	N_{ELI} [e]	V_{ELI} [Å^3]	γ_{ELI}	RJI [%]
N(1)–N(2)	0.51	−0.81	1.15	0.8	1.56	50.6
P(1)–N(1)	1.21	−0.99	1.79	2.6	1.67	82.5
P(2)–N(2)	1.31	−0.99	1.84	2.9	1.66	81.7
Si(1)–N(1)	1.32	−0.52	2.46	4.8	1.75	93.9
Si(2)–N(2)	1.39	−0.52	2.85	5.6	1.73	94.5
2 a(2)	$G/\varrho(\mathbf{r})_{bcp}$ [a.u.]	$H/\varrho(\mathbf{r})_{bcp}$ [a.u.]	N_{ELI} [e]	V_{ELI} [Å^3]	γ_{ELI}	RJI [%]
N(1)–N(2)	0.51	−0.89	1.14	0.8	1.56	54.6
P(1)–N(1)	1.55	−0.80	1.94	3.2	1.67	83.4
P(2)–N(2)	1.52	−0.82	1.93	3.1	1.67	82.3
Si(1)–N(1)	1.63	−0.35	2.53	4.6	1.74	93.8
B(2)–N(2)	1.30	−0.77	2.37	4.0	1.84	93.4

[a] Bond distances in Å, angles and torsion angles in °, high: 6–311 + G(2df,p), low: 6–31 + G*, $\varrho(\mathbf{r})_{bcp}$: ED at the bcp, $\nabla^2\varrho(\mathbf{r})_{bcp}$: Laplacian, ε: bond ellipticity d_1: distance atom(1)-bcp, Q(E): AIM charge of element E (E=N, P, Si/B), $G/\varrho(\mathbf{r})_{bcp}$, $H/\varrho(\mathbf{r})_{bcp}$: kinetic and total energy density over $\varrho(\mathbf{r})_{bcp}$ ratios, N_{ELI}, V_{ELI}: electron populations and volumes the ELI–D basin, γ_{ELI}: ELI–D value at the attractor position, RJI: Raub-Jansen Index. Values for the Si_2P_2-systems stem from ref. [38].

electronically (and thus energetically), splitting the N–N bond becomes feasible. The absolute size of the N–N bonding basin is displayed in Figure 3d. The ELI–D distribution on the basin surface has (purple) maxima pointing along the other basin directions.

Conclusions

According to our results (see also reference 38) for light-atom small-molecule design in the field of N_2 to NH_3 conversion with a single molecule, the following eight points are crucial:

a) All four binding partners for N_2 should be arranged in an as-close-as-possible tetrahedral-like fashion to provide a polarized binding pocket.
b) Only an A_2B_2-pocket with two Lewis acids (A) and two Lewis bases (B) is capable of energy efficient N_2-fixation. It can't be replaced by A_4-, A_3B-, AB_3-, or B_4-pockets.

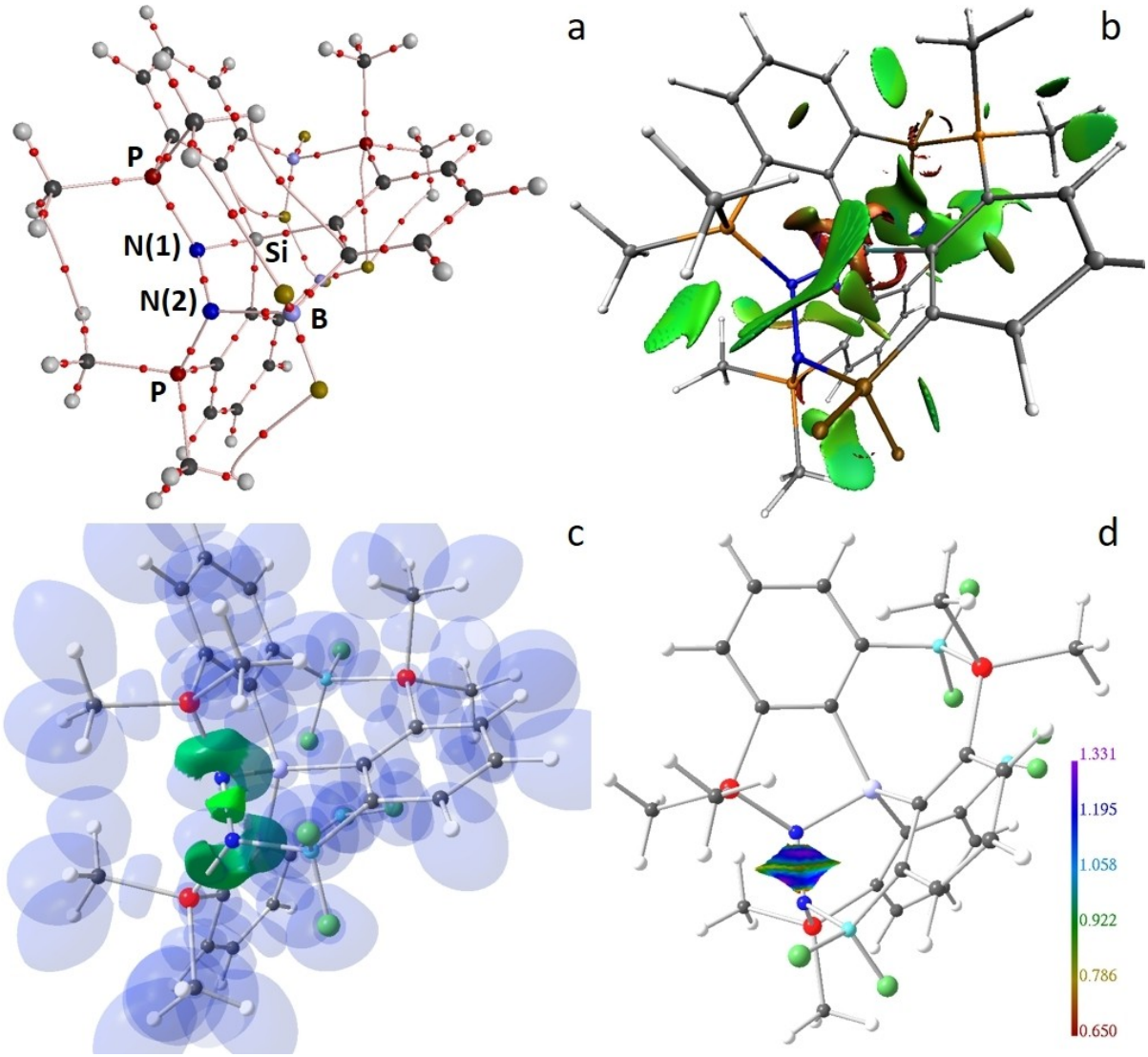

Figure 3. RSBI analysis of **2 a(2)**. a) AIM bond paths motif, b) NCI iso-surface at s(r) = 0.5, c) ELI–D localization domain representation at iso-value of 1.3, d) ELI–D distribution mapped on the N–N ELI–D bonding basin. Color code atoms: hydrogen – light gray, carbon – medium gray, phosphor – orange or red, silicon – light blue or gray, fluorine – green or brown, boron – light blue or brownish.

c) Symmetric ABN–NBA coordination is superior over A_2N–NB_2 coordination.
d) The ligand system needs a certain degree of flexibility to accommodate for the electronic and structural changes in the N_2-binding area. However, for entropic reasons, the flexibility needs to be limited.
e) If $Si^{(+)}$ centers are employed for N_2-fixation, quenching of the activator molecule after initial hydride abstraction has to be prevented by purging the solution with gaseous N_2.
f) Silicon cations can only be replaced by the less electrophilic boron if N_2-fixation is supported by additional intramolecular secondary interactions, such as P–B or F···B dative bonds, outside the binding pocket, without initially quenching the starting state.
g) Phosphor can't be replaced by nitrogen or arsenic, as the specific "softness" of phosphor in donating and accepting electrons is crucial for N_2-fixation and activation.
h) Detrimental protonation of "free" $-PMe_2$ groups has to be considered as these side-reactions might hamper further N_2-reduction. Undesired addition of hydride to "free" $-BF_2$ groups should be much less critical. However, potential fluoride abstraction from $-BF_2$ groups has to be considered if $Si^{(+)}$ centers are employed.

Taking these considerations into account, it should be possible to design a light atom molecular system which can facilitate full N_2 to NH_3 conversion and is accessible by synthetic chemistry.

Acknowledgements

Prof. Dr. Jens Beckmann is greatly acknowledged for helpful discussions and critically reading the manuscript. The DFG is acknowledged for funding. Open Access funding enabled and organized by Projekt DEAL.

Conflict of Interest

The authors declare no conflict of interest.

Data Availability Statement

The data that support the findings of this study are available from the corresponding author upon reasonable request.

Keywords: density functional calculations · frustrated Lewis pairs · nitrogen splitting · *peri*-substituted systems · real-space bonding indicators

[1] R. E. Blankenship, *Molecular mechanisms of photosynthesis*, Third edition. ed., Wiley, Hoboken, **2022**.
[2] A. M. Appel, J. E. Bercaw, A. B. Bocarsly, H. Dobbek, D. L. DuBois, M. Dupuis, J. G. Ferry, E. Fujita, R. Hille, P. J. A. Kenis, C. A. Kerfeld, R. H. Morris, C. H. F. Peden, A. R. Portis, S. W. Ragsdale, T. B. Rauchfuss, J. N. H. Reek, L. C. Seefeldt, R. K. Thauer, G. L. Waldrop, *Chem. Rev.* **2013**, *113*, 6621–6658.
[3] B. M. Hoffman, D. Lukoyanov, Z. Y. Yang, D. R. Dean, L. C. Seefeldt, *Chem. Rev.* **2014**, *114*, 4041–4062.
[4] N. Gruber, J. N. Galloway, *Nature* **2008**, *451*, 293–296.
[5] IEDT, *Vol. 2021*, Industrial Efficiency Technology Database.
[6] Q. Wang, D. Astruc, *Chem. Rev.* **2020**, *120*, 1438–1511.
[7] S. S. Liu, M. F. Wang, T. Qian, H. Q. Ji, J. Liu, C. L. Yan, *Nat. Commun.* **2019**, *10*.
[8] J. X. Zhao, Z. F. Chen, *J. Am. Chem. Soc.* **2017**, *139*, 12480–12487.
[9] X. Mao, S. Zhou, C. Yan, Z. H. Zhu, A. J. Du, *Phys. Chem. Chem. Phys.* **2019**, *21*, 1110–1116.
[10] C. V. S. Kumar, V. Subramanian, *Phys. Chem. Chem. Phys.* **2017**, *19*, 15377–15387.
[11] W. B. Qiu, X. Y. Xie, J. D. Qiu, W. H. Fang, R. P. Liang, X. Ren, X. Q. Ji, G. W. Cui, A. M. Asiri, G. L. Cui, B. Tang, X. P. Sun, *Nat Commun* **2018**, *9*.
[12] M. Zheng, Y. Li, K. N. Ding, Y. F. Zhang, W. K. Chen, W. Lin, *J. Mater. Chem. A* **2020**, *8*, 7412–7421.
[13] M. Zafari, D. Kumar, M. Umer, K. S. Kim, *J. Mater. Chem. A* **2020**, *8*, 5209–5216.
[14] S. B. Tang, Q. Dang, T. Y. Liu, S. Y. Zhang, Z. G. Zhou, X. K. Li, X. J. Wang, E. Sharman, Y. Luo, J. Jiang, *J. Am. Chem. Soc.* **2020**, *142*, 19308–19315.
[15] P. Sun, J. Huang, F. Xu, J. J. Xu, T. Q. Lin, W. Zhao, W. J. Dong, F. Q. Huang, *ACS Appl. Mater. Interfaces* **2020**, *12*, 28075–28082.
[16] B. Liu, Y. P. Zheng, H. Q. Peng, B. F. Ji, Y. Yang, Y. B. Tang, C. S. Lee, W. J. Zhang, *ACS Energy Lett.* **2020**, *5*, 2590–2596.
[17] C. W. Liu, Q. Y. Li, C. Z. Wu, J. Zhang, Y. G. Jin, D. R. MacFarlane, C. H. Sun, *J. Am. Chem. Soc.* **2019**, *141*, 2884–2888.
[18] T. Y. Liu, Q. Dang, X. H. Zhou, J. Li, Z. Ge, H. Che, S. B. Tang, Y. Luo, J. Jiang, *Chem. Eur. J.* **2021**, *27*, 6945–6953.
[19] S. F. Ye, E. Bill, F. Neese, *Inorg. Chem.* **2016**, *55*, 3468–3474.
[20] B. D. Matson, J. C. Peters, *ACS Catal.* **2018**, *8*, 1448–1455.
[21] M. P. Shaver, M. D. Fryzuk, *Adv. Synth. Catal.* **2003**, *345*, 1061–1076.
[22] J. B. Lu, X. L. Wang, J. Q. Wang, J. C. Liu, H. Xiao, J. Li, *J. Phys. Chem. A* **2018**, *122*, 4530–4537.
[23] A. Eizawa, K. Arashiba, H. Tanaka, S. Kuriyama, Y. Matsuo, K. Nakajima, K. Yoshizawa, Y. Nishibayashi, *Nat. Commun.* **2017**, *8*.
[24] Y. Ashida, Y. Nishibayashi, *Chem. Commun.* **2021**, *57*.
[25] J. Fajardo, J. C. Peters, *Inorg. Chem.* **2021**, *60*, 1221–1228.
[26] C. N. Tang, Q. M. Liang, A. R. Jupp, T. C. Johnstone, R. C. Neu, D. T. Song, S. Grimme, D. W. Stephan, *Angew. Chem. Int. Ed.* **2017**, *56*, 16588–16592; *Angew. Chem.* **2017**, *129*, 16815–16819.
[27] I. Mallov, A. J. Ruddy, H. Zhu, S. Grimme, D. W. Stephan, *Chem. Eur. J.* **2017**, *23*, 17692–17696.
[28] R. L. Melen, *Angew. Chem. Int. Ed.* **2018**, *57*, 880–882; *Angew. Chem.* **2018**, *130*, 890–892.
[29] A. J. Ruddy, D. M. C. Ould, P. D. Newman, R. L. Melen, *Dalton Trans.* **2018**, *47*, 10377–10381.
[30] C. Hering-Junghans, *Angew. Chem. Int. Ed.* **2018**, *57*, 6738–6740; *Angew. Chem.* **2018**, *130*, 6850–6852.
[31] M. A. Legare, G. Belanger-Chabot, R. D. Dewhurst, E. Welz, I. Krummenacher, B. Engels, H. Braunschweig, *Science* **2018**, *359*, 896–899.
[32] M. A. Legare, M. Rang, G. Belanger-Chabot, J. I. Schweizer, I. Krummenacher, R. Bertermann, M. Arrowsmith, M. C. Holthausen, H. Braunschweig, *Science* **2019**, *363*, 1329–1332.
[33] L. L. Cao, J. L. Zhou, Z. W. Qu, D. W. Stephan, *Angew. Chem. Int. Ed.* **2019**, *58*, 18487–18491; *Angew. Chem.* **2019**, *131*, 18658–18662.
[34] D. Mandal, T. Chen, Z. W. Qu, S. Grimme, D. W. Stephan, *Angew. Chem. Int. Ed.* **2022**, *61*, e20220924.
[35] D. Y. Zhu, Z. W. Qu, D. W. Stephan, *Dalton Trans.* **2020**, *49*, 901–910.
[36] L. F. Li, Z. Y. Wu, H. J. Zhu, G. H. Robinson, Y. M. Xie, H. F. Schaefer, *J. Am. Chem. Soc.* **2020**, *142*, 6244–6250.
[37] D. Y. Zhu, Z. W. Qu, J. L. Zhou, D. W. Stephan, *Chem. Eur. J.* **2021**, *27*, 2861–2867.
[38] S. Mebs, J. Beckmann, *Phys. Chem. Chem. Phys.* **2022**, *24*, 20953–20967.
[39] R. F. W. Bader, *B Am Phys Soc* **1977**, *22*, 305–306.
[40] R. F. W. Bader, T. T. Nguyendang, *Adv. Quantum Chem.* **1981**, *14*, 63–124.
[41] R. F. W. Bader, *Accounts Chem Res* **1985**, *18*, 9–15.
[42] E. R. Johnson, S. Keinan, P. Mori-Sanchez, J. Contreras-Garcia, A. J. Cohen, W. T. Yang, *J. Am. Chem. Soc.* **2010**, *132*, 6498–6506.
[43] M. Kohout, *Int. J. Quantum Chem.* **2004**, *97*, 651–658.
[44] A. D. Becke, *J. Chem. Phys.* **1993**, *98*, 1372–1377.
[45] J. P. Perdew, J. A. Chevary, S. H. Vosko, K. A. Jackson, M. R. Pederson, D. J. Singh, C. Fiolhais, *Phys. Rev. B* **1992**, *46*, 6671–6687.
[46] Gaussian 16 (Revision C.01), M. J. Frisch, G. W. Trucks, H. B. Schlegel, G. E. Scuseria, M. A. Robb, J. R. Cheeseman, G. Scalmani, V. Barone, G. A. Petersson, H. Nakatsuji, X. Li, M. Caricato, A. V. Marenich, J. Bloino, B. G. Janesko, R. Gomperts, B. Mennucci, H. P. Hratchian, J. V. Ortiz, A. F. Izmaylov, J. L. Sonnenberg, D. Williams-Young, F. Ding, F. Lipparini, F. Egidi, J. Goings, B. Peng, A. Petrone, T. Henderson, D. Ranasinghe, V. G. Zakrzewski, J. Gao, N. Rega, G. Zheng, W. Liang, M. Hada, M. Ehara, K. Toyota, R. Fukuda, J. Hasegawa, M. Ishida, T. Nakajima, Y. Honda, O. Kitao, H. Nakai, T. Vreven, K. Throssell, J. A. Montgomery, Jr., J. E. Peralta, F. Ogliaro, M. J. Bearpark, J. J. Heyd, E. N. Brothers, K. N. Kudin, V. N. Staroverov, T. A. Keith, R. Kobayashi, J. Normand, K. Raghavachari, A. P. Rendell, J. C. Burant, S. S. Iyengar, J. Tomasi, M. Cossi, J. M. Millam, M. Klene, C. Adamo, R. Cammi, J. W. Ochterski, R. L. Martin, K. Morokuma, O. Farkas, J. B. Foresman, D. J. Fox, Gaussian, Inc., Wallingford CT, **2016**.
[47] S. Grimme, *J. Comput. Chem.* **2006**, *27*, 1787–1799.
[48] S. Miertus, E. Scrocco, J. Tomasi, *Chem. Phys.* **1981**, *55*, 117–129.
[49] C. J. Cramer, *Essentials of Computational Chemistry: Theories and Models*, 2nd ed., Wiley & Sons Ltd, **2004**.
[50] F. Biegler-Konig, J. Schonbohm, D. Bayles, *J. Comput. Chem.* **2001**, *22*, 545–559.
[51] M. Kohout , *Vol. Radebeul*, 4.6 ed., **2015**.
[52] J. Contreras-Garcia, E. R. Johnson, S. Keinan, R. Chaudret, J. P. Piquemal, D. N. Beratan, W. T. Yang, *J. Chem. Theory Comput.* **2011**, *7*, 625–632.
[53] G. A. Andirenko, 1.8 ed., CrowdStrike, https://www.chemcraftprog.com.
[54] W. Humphrey, A. Dalke, K. Schulten, *J. Mol. Graphics Modell.* **1996**, *14*, 33–38.
[55] C. B. Hübschle, P. Luger, *J. Appl. Crystallogr.* **2006**, *39*, 901–904.
[56] S. Mebs, *Chem. Phys. Lett.* **2016**, *651*, 172–177.
[57] S. Raub, G. Jansen, *Theor. Chem. Acc.* **2001**, *106*, 223–232.

Manuscript received: August 18, 2022
Revised manuscript received: November 20, 2022
Accepted manuscript online: November 23, 2022
Version of record online: December 13, 2022